THE ASTROPHYSICAL JOURNAL, 503:729–743, 1998 August 20
© 1998. The American Astronomical Society. All rights reserved. Printed in U.S.A.

# THE MULTIPHASE MEDIUM IN THE INTERSTELLAR COMPLEX N44

SUNGEUN KIM,[1] YOU-HUA CHU,[2] LISTER STAVELEY-SMITH,[3] AND R. CHRIS SMITH[4]

*Received 1997 August 21; accepted 1998 April 1*

## ABSTRACT

We have obtained high-resolution H I observations of N44, one of the largest H II complexes in the Large Magellanic Cloud. The distribution and internal motions of the H I gas show dynamic effects of fast stellar winds and supernova blasts. Numerous H I holes are detected, with the most prominent two corresponding to the optically identified superbubbles Shell 1 and Shell 2. The H I gas associated with Shell 1 shows an expansion pattern similar to that of the ionized gas shell, but the mass and kinetic energy of the H I shell are 3–7 times those of the ionized gas shell. The total kinetic energy of the neutral and ionized gas of Shell 1 is still more than a factor of 5 lower than expected in a pressure-driven superbubble. It is possible that the central OB association was formed in a molecular cloud, and a visible superbubble was not fully developed until the ambient molecular gas had been dissociated and cleared away. This hypothesis is supported by the existence of a molecular cloud toward N44 and the fact that the apparent dynamic age of the superbubble Shell 1 is much shorter than the age of its OB association LH 47. Accelerated H I gas is detected at SNR 0523−679. The mass and kinetic energy in the associated H I gas are also much higher than those in the ionized gas of SNR 0523−679. Studies of interstellar gas dynamics using ionized gas alone are clearly inadequate; neutral gas components *must* be included.

*Subject headings:* H II regions — ISM: bubbles — ISM: individual (N44) — Magellanic Clouds — supernova remnants

## 1. INTRODUCTION

N44, cataloged by Henize (1956), is a luminous H II complex in the Large Magellanic Cloud (LMC). It contains an assortment of compact H II regions, filaments, and shells of all sizes, as well as three OB associations, LH 47, LH 48, and LH 49 (Lucke & Hodge 1970). As shown in Figure 1, N44 is dominated by a prominent shell around LH 47 in the central region (Chu & Mac Low 1990). In the surroundings are diffuse H II regions and filaments to the east; compact H II regions encompassing LH 49 to the south; a large faint shell to the west; faint filaments to the north; a luminous, compact H II region around LH 48 on the northeastern rim of the main shell; and numerous small, bright single-star H II regions in the outskirts of N44.

Previous studies of ionized gas in N44 have yielded many interesting results. The main shell and the large shell to the west are designated as Shells 1 and 2, respectively, and their expansion patterns have been studied by Meaburn & Laspias (1991). Shell 1 has been modeled as a superbubble using energy input implied by the observed massive stellar content; it is shown that the expansion velocity of Shell 1 is much higher than expected (Oey & Massey 1995). Diffuse X-ray emission has been detected in N44, indicating the existence of $10^6$ K gas (Chu & Mac Low 1990; Wang & Helfand 1991). The X-ray emission within Shells 1 and 2 has been suggested to be generated by supernova remnants (SNRs) shocking the shell walls; the outward extension of X-ray emission at the southern periphery of Shell 1 has been interpreted as a breakout; and the bright diffuse X-ray source at 6′–7′ northeast of Shell 1 has been identified as a new SNR (Chu et al. 1993; Magnier et al. 1996). Following the naming convention of using truncated B1950 coordinates, this remnant will be named SNR 0523−679.

Interactions between massive stars and the interstellar medium (ISM) have led to the derivation of a multiphase ISM model (McKee & Ostriker 1977) and have been used to explain the disk-halo connection in a galaxy (Norman & Ikeuchi 1989). The physical structure of N44 vividly demonstrates the dynamical interaction between massive stars and the ISM. Thus, N44 provides an excellent laboratory to study in detail the distribution, physical conditions, and relationship of the different phases of the ISM in a star-forming region.

Previous studies of N44 have concentrated only on the warm and hot ionized gas. In order to carry out a comprehensive investigation of the multiphase structure of N44, we have recently obtained high-resolution H I observations of N44 with the Australia Telescope Compact Array (ATCA) and high-dispersion, long-slit echelle spectra of N44 with the 4 m telescope at Cerro Tololo Inter-American Observatory. In this paper we report these observations (§ 2), describe the interaction between H I and H II gases (§ 3), analyze the H I gas associated with Shell 1 and Shell 2 (§ 4), and study the acceleration of H I gas by a SNR (§ 5). A discussion is given at the end (§ 6).

## 2. OBSERVATIONS

### 2.1. H I *Observations*

The H I data of N44 are extracted from the H I aperture synthesis survey of the LMC made with the Australia Telescope Compact Array (ATCA), which consists of six 22 m antennas. The details of this survey are given by Kim et al. (1998), and preliminary results are presented by Kim & Staveley-Smith (1997).

In summary, the observations were made in four configurations: 750A on 1995 February 23–March 11, 750B on

[1] Mount Stromlo and Siding Spring Observatories, ANU, Weston Creek Post Office, Canberra, ACT 2611, Australia.
[2] Astronomy Department, University of Illinois at Urbana-Champaign, Urbana, IL 61801.
[3] Australia Telescope National Facility, CSIRO, P.O. Box 76, Epping, NSW 2121, Australia.
[4] Astronomy Department, University of Michigan, Ann Arbor, MI 48109-1090.

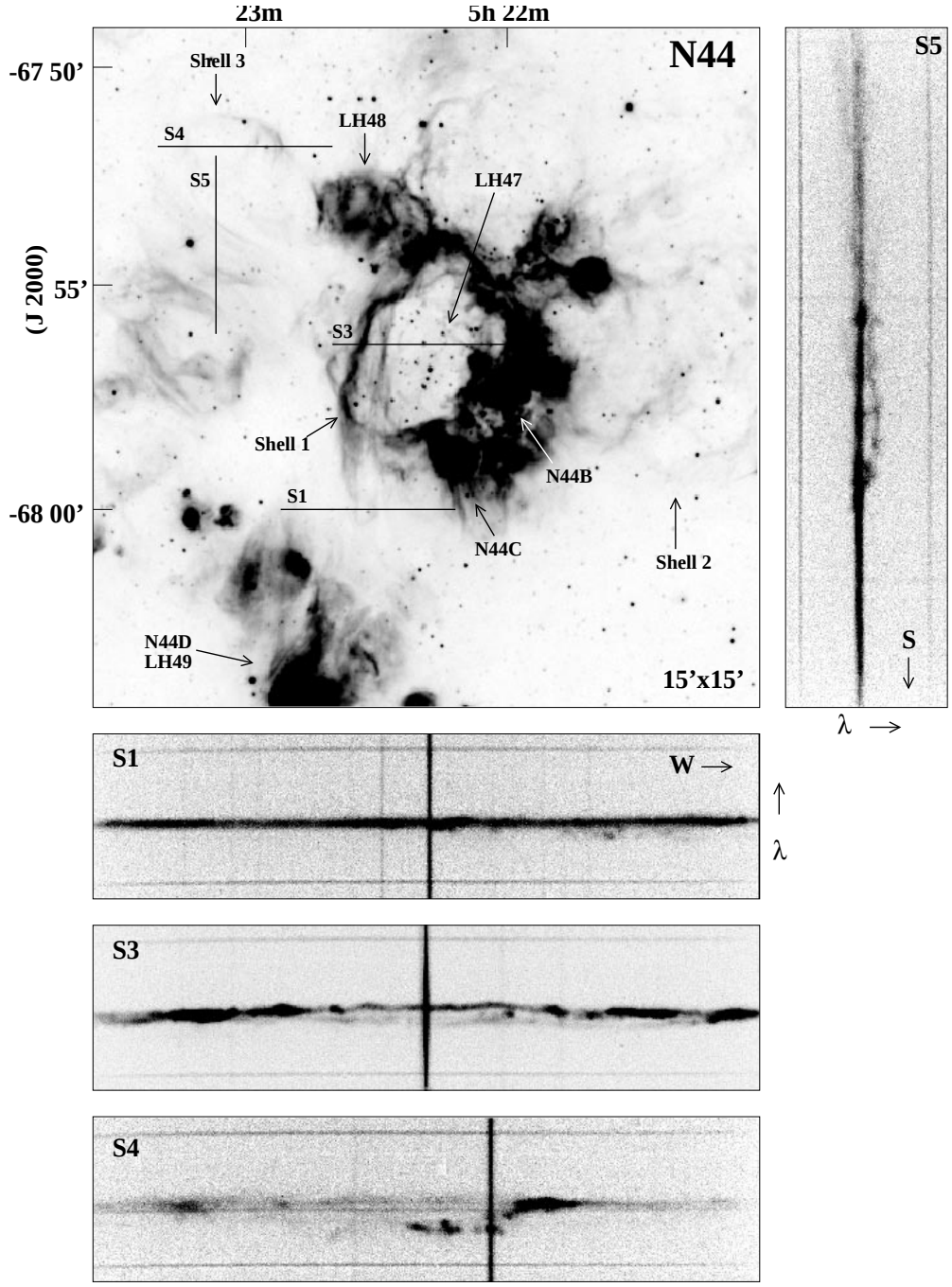



FIG. 1.—Hα image of the N44 complex and echellograms. The echelle slit positions are marked in the Hα image. The slit S3 samples the center of the superbubble Shell 1. The slit S1 samples the breakout region, or the X-ray South Bar (Magnier et al. 1996). S4 and S5 sample the lobes of the SNR 0523−679. The two narrow lines in the echellograms are the geocoronal Hα and the telluric OH line blend at 6577.284 Å.

1996 January 27–February 8, 750C on 1995 October 15–31, and 750D on 1994 October 26–November 9. These configurations each have five antennas with a maximum baseline of 750 m. The combined configuration has 40 independent baselines ranging from 30 to 750 m, with a baseline increment of 15.3 m. The resultant angular resolution is 1.0 for the H I images presented in this paper. The largest angular structure that the images are sensitive to is ∼0.6.

The observing band was centered at 1.419 GHz with a bandwidth of 4 MHz. The band was divided into 1024 channels; these channels were rebinned into 400 channels after an online application of Hanning smoothing and edge rejection. The final data cube used here has a velocity coverage of 190–387 km $s^{-1}$ and a velocity resolution of 1.65 km $s^{-1}$. All H I and Hα velocities reported in this paper are heliocentric.

The data cube of N44 was extracted from the full mosaic of the LMC, which consisted of 1344 pointing centers. Approximately four pointing centers were included in the data cube of N44. The phase and amplitude calibrators were PKS B0407−658 for some fields and PKS B0454−810 for the others. The primary ATCA calibrator, PKS B1934−638 (assumed flux density 14.9 Jy at 1.419 GHz), was observed at the start and end of each observing day. These observations served both for bandpass calibration and flux density calibration.

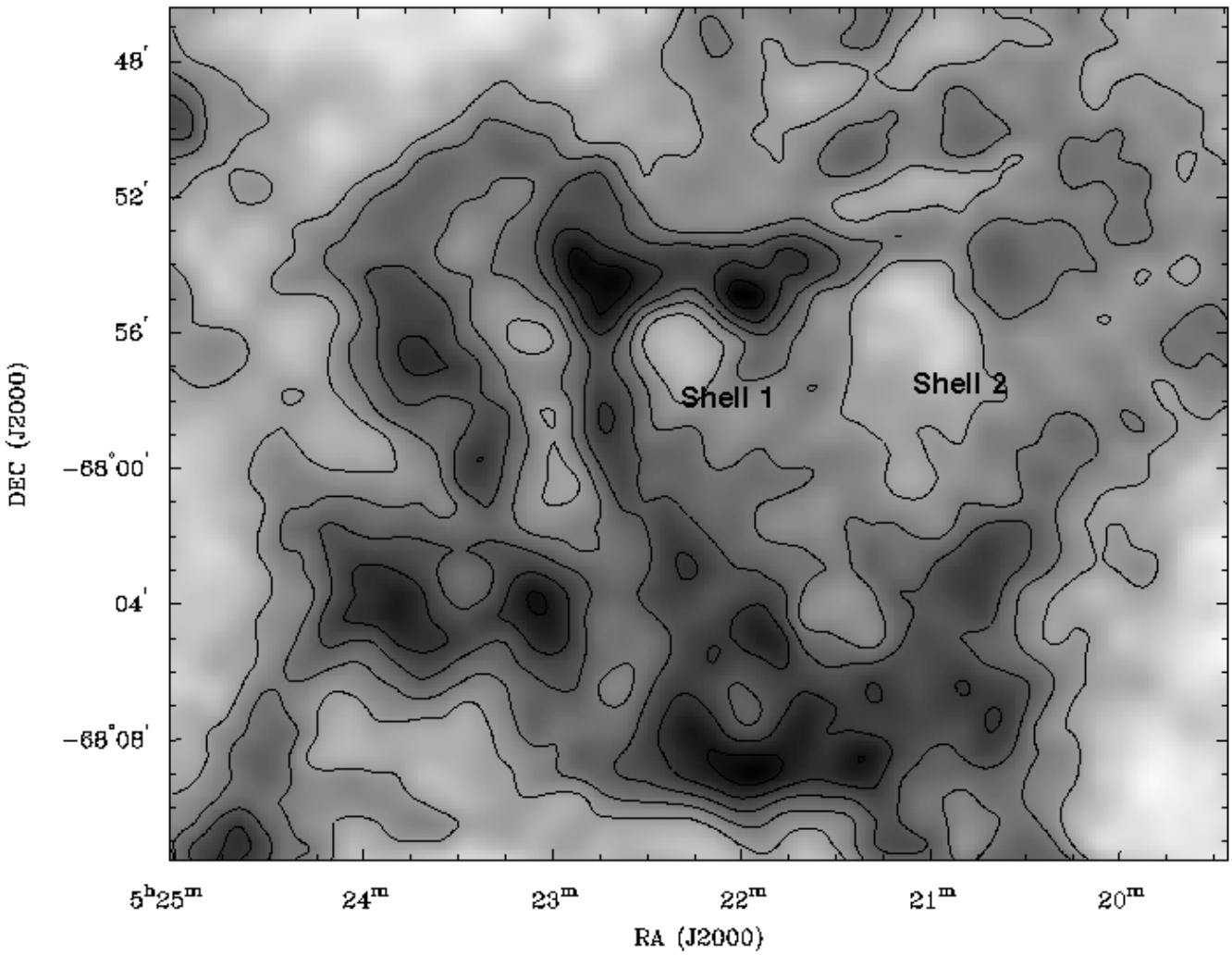



FIG. 2a

FIG. 2.—ATCA integrated H I map of the N44 complex. The optically defined Shells 1 and 2 are labeled on the H I contours (*a*) on gray-scale images of H I themselves and (*b*) on H I (light-green) images with an Hα (red) image. Corresponding H I holes in these positions can be clearly seen.

The data were edited, calibrated, and mosaicked in MIRIAD. The pixel size is 20″, and the size of the N44 cube is 23 × 23 × 120. Superuniform weighting (Sramek & Schwab 1989) was applied to the *uv* data with an additional Gaussian taper. The resulting data were then Fourier transformed and mosaicked in the image plane. The maximum entropy method was used to deconvolve this cube. The final cube was constructed by convolving the maximum entropy model with a Gaussian of FWHM 1′ × 1′. The final rms noise, measured in line-free parts of the final cube, is 9 K.

### 2.2. *Echelle Observations*

To examine the kinematic properties of the ionized gas in N44, we obtained high-dispersion spectroscopic observations in the Hα + [N II] lines with the echelle spectrograph on the 4 m telescope at Cerro Tololo Inter-American Observatory on 1995 January 18. Using a postslit Hα filter and replacing the cross-disperser with a flat mirror, we were able to observe both Hα and [N II] λλ6548, 6583 lines over a long slit. The 79 lines $mm^{-1}$ echelle grating and the red long-focus camera were used. The data were recorded with a Tek 2048 × 2048 CCD. The 24 μm pixel size corresponds to about 0.82 Å (3.75 km $s^{-1}$ at the Hα line) along the spectral direction and 0.″267 along the spatial direction. The spectral coverage was limited by the filter width to 125 Å. The spatial coverage was limited by the slit length to ∼4′, with some vignetting in the outer 1.′5. The slit width was 250 μm, or 1.″66, and the instrumental FWHM was 16.1 ± 0.8 km $s^{-1}$.

The wavelength calibration and geometric distortion correction were carried out with the use of Th-Ar lamp exposures in the beginning of the night. The observations were sufficiently deep that the geocoronal Hα component was detected in each frame. The geocoronal Hα component (at zero observed velocity) provided an accurate and convenient reference for velocity measurements. The observed velocities were then converted to heliocentric velocities.

The journal of echelle observations is given in Table 1, and the echellograms are shown in Figure 1. Only the Hα line is presented in the echellograms. The [N II] lines are detected at a much lower S/N ratio than the Hα line, hence they are not presented here.

### 2.3. *Optical Imaging*

In order to compare the neutral gas components to the ionized gas in the N44 region, we obtained optical Hα emission-line images with a CCD camera mounted at the Newtonian focus of the Curtis Schmidt telescope at CTIO

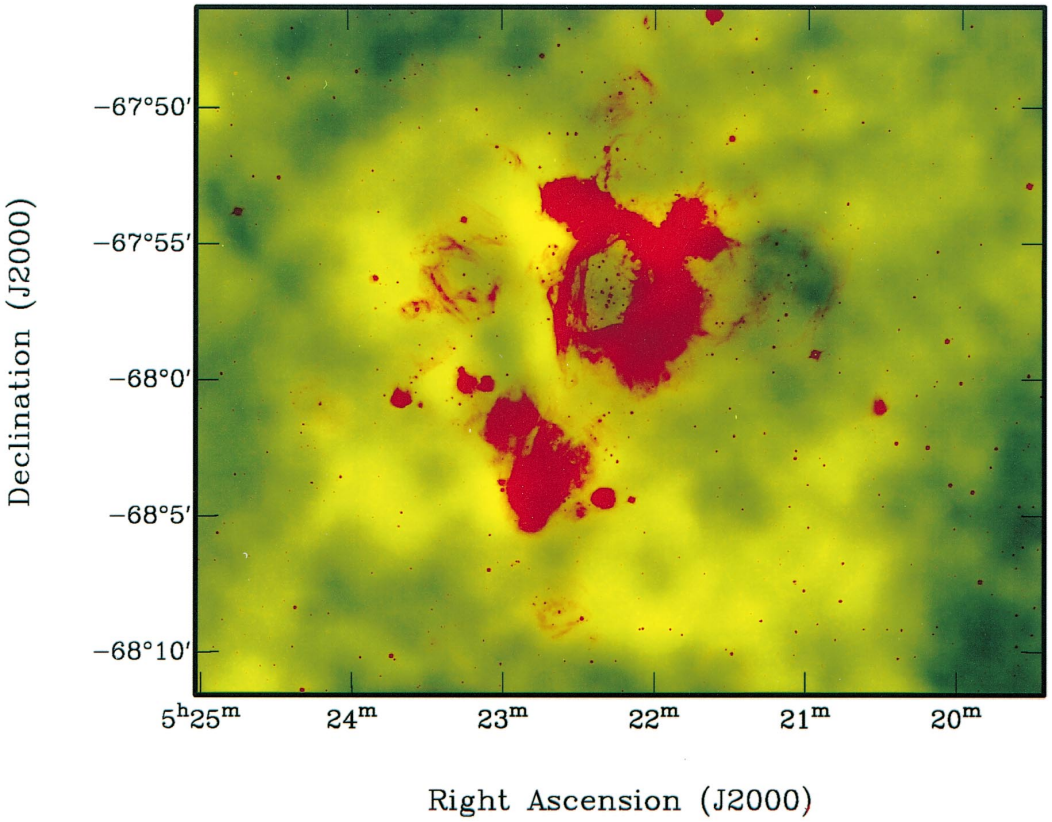



FIG. 2*b*

TABLE 1

JOURNAL OF ECHELLE OBSERVATIONS

| Number | R.A. (J2000) | Decl. (J2000) | Slit Orientation | Exposure (s) | Remarks |
|---|---|---|---|---|---|
| 1..... | 05 22 32 | −68 00 06 | E-W | 1200 | South breakout region |
| 2..... | 05 22 32 | −68 00 46 | E-W | 1200 | 40″ S of slit 1 |
| 3..... | 05 22 17 | −67 56 18 | E-W | 2 × 1200 | Center of Shell 1 |
| 4..... | 05 23 01 | −67 52 02 | E-W | 2 × 1200 | SNR |
| 5..... | 05 23 05 | −67 54 09 | N-S | 2 × 1200 | SNR |
| 6..... | 05 22 32 | −68 00 26 | E-W | 1200 | 20″ S of slit 1 |

NOTE.—Units of right ascension are hours, minutes, and seconds, and units of declination are degrees, arcminutes, and arcseconds.

on 1994 February 18 UT. The detector was a front-illuminated Thomson 1024 × 1028 CCD with 19 $\mu$m pixels, giving a scale of 1.″835 pixel$^{-1}$ and a field of view of 31.′3. A narrow-bandpass H$\alpha$ filter ($\lambda_c = 6561$ Å, $\Delta\lambda = 26$ Å) was used to isolate the emission, and a red continuum filter ($\lambda_c = 6840$ Å, $\Delta\lambda = 95$ Å) was used to obtain images of the continuum background (images in other emission lines were also obtained, but those will be discussed in another paper). Multiple frames were obtained through each filter, amounting to total integration times of 1200 s in H$\alpha$ and 600 s in the continuum. The data were reduced with IRAF,[5] and multiple frames were shifted and combined to obtain the images shown in Figures 1 and 3*b*.

## 3. INTERACTION BETWEEN H I AND H II COMPONENTS

The integrated H I map of N44 (Fig. 2) shows two clear depressions that correspond to the interiors of the optically defined Shell 1 and Shell 2, and peaks that are adjacent to H$\alpha$ features. The relationship between the H I gas and the H II gas is clearly complex. The ATCA channel maps of H I (Fig. 3*a*) kinematically resolve the distribution of H I along the line of sight and allow more precise identification of physical structures in the H I distribution. Comparing these isovelocity maps of H I to the H$\alpha$ image (Fig. 3*b*), we may examine the relationship between the H I and H II gas in greater detail and accuracy.

From the comparisons of H I and H$\alpha$ images, we have found indications of (1) H I holes and expanding shells, (2) acceleration of H I, (3) compression of H I, and (4) the opening of a breakout in H I. These phenomena are described below in more detail.

[5] IRAF is distributed by the National Optical Astronomy Observatories (NOAO).

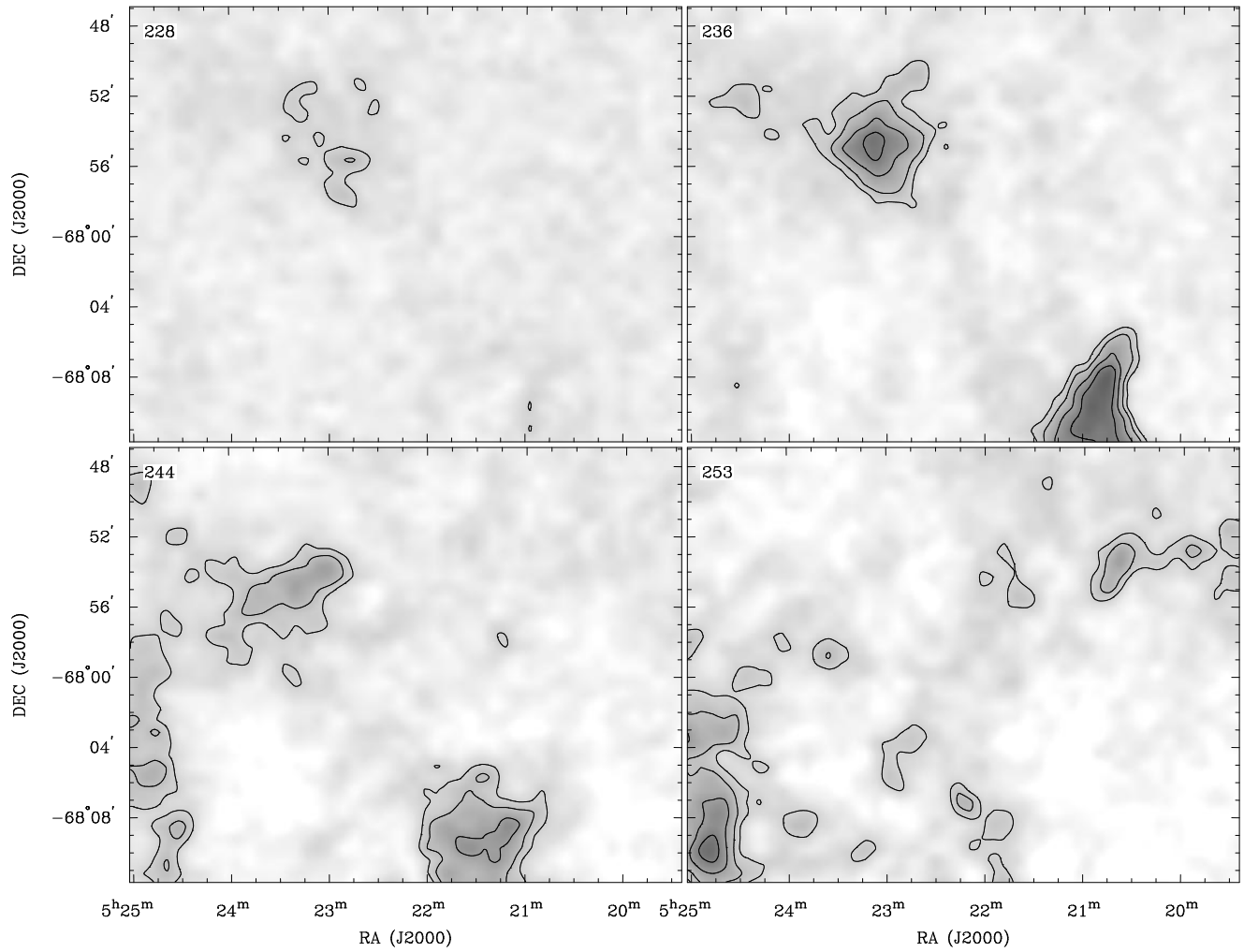



FIG. 3a

FIG. 3.—ATCA channel maps of N44's H I data cube. The heliocentric velocity is given in the upper left corner. The H I contours are overplotted (*a*) on gray-scale images of H I themselves and (*b*) on an Hα image. The contour levels are 0.07, 0.10, 0.15, 0.20, 0.25, 0.30, 0.35, 0.40, and 0.45 Jy beam$^{-1}$.

### 3.1. H I *Holes and Expanding Shells*

The Hα image in Figure 1 reveals the prominent superbubble Shell 1 and the fainter superbubble Shell 2 in N44. Shell 1, around the OB association LH 47, has a size of 70 pc × 50 pc, while Shell 2, with no obvious OB association inside, is 60 pc across. The H I channel maps at $V_{\rm hel}$ = 292–302 km s$^{-1}$ (Fig. 3) show clear H I holes at the central cavities of Shell 1 and Shell 2. Projected within the H I holes are high-velocity H I clumps (∼15 pc diameter) at $5^{\rm h}22^{\rm m}15^{\rm s}$, −67°56′40″ (J2000) at the velocity range of $V_{\rm hel}$ ∼ 240–250 km s$^{-1}$ (see Fig. 3). These high-velocity H I clumps are most likely the brightest parts of the approaching hemisphere of an expanding H I shell associated with the optical shell. The receding hemispheres of these shells expand more slowly. The expansion of these H I shells is better visualized in the position-velocity plots (or *L*-*V* diagrams) in Figure 4. These shells will be analyzed in detail in § 4.

Besides the H I shells with obvious optical counterparts, we see two H I holes, centered at $V_{\rm hel}$ = 297 km s$^{-1}$, without known expanding shells in the optical. Inspected closely, the H I hole at $5^{\rm h}22^{\rm m}00^{\rm s}$, −67°51′50″ (J2000) is associated with sharp, curved optical filaments that appear to delineate a shell structure, while the H I hole at $5^{\rm h}21^{\rm m}07^{\rm s}$, −67°51′45″ (J2000) appears to be associated only with faint, irregular optical filaments. Interestingly, as shown in Figure 5, both of these H I holes encompass regions of bright diffuse X-ray emission reported by Chu et al. (1993). The relationship between the X-ray–emitting ionized gas and the H I gas will be discussed further in § 6.

### 3.2. *Acceleration of* H I

The H I channel maps in Figure 3 show that the bulk of H I gas is detected in the velocity range of 295–305 km s$^{-1}$. High-velocity H I gas with $\Delta V$ up to −80 km s$^{-1}$ is detected in a portion of SNR 0523−679. This high-velocity gas must have been accelerated by the SNR. High-velocity H I gas ($V_{\rm hel}$ = 233 km s$^{-1}$) is also detected in the region between the SNR and the superbubble Shell 1. This gas might consist of two components, one accelerated by the SNR and the other by Shell 1, as the H I contours have an excellent correspondence with an Hα blister on the periphery of Shell 1 .

### 3.3. *Compression of* H I

In the channel maps near the bulk velocity, H I peaks are seen in regions between expanding H I shells. It is possible that these peaks represent compressions caused by two shells expanding into each other. One example is the region at $5^{\rm h}22^{\rm m}40^{\rm s}$, −67°54′40″ (J2000) between SNR 0523−679 and the superbubble Shell 1; the H I column density,

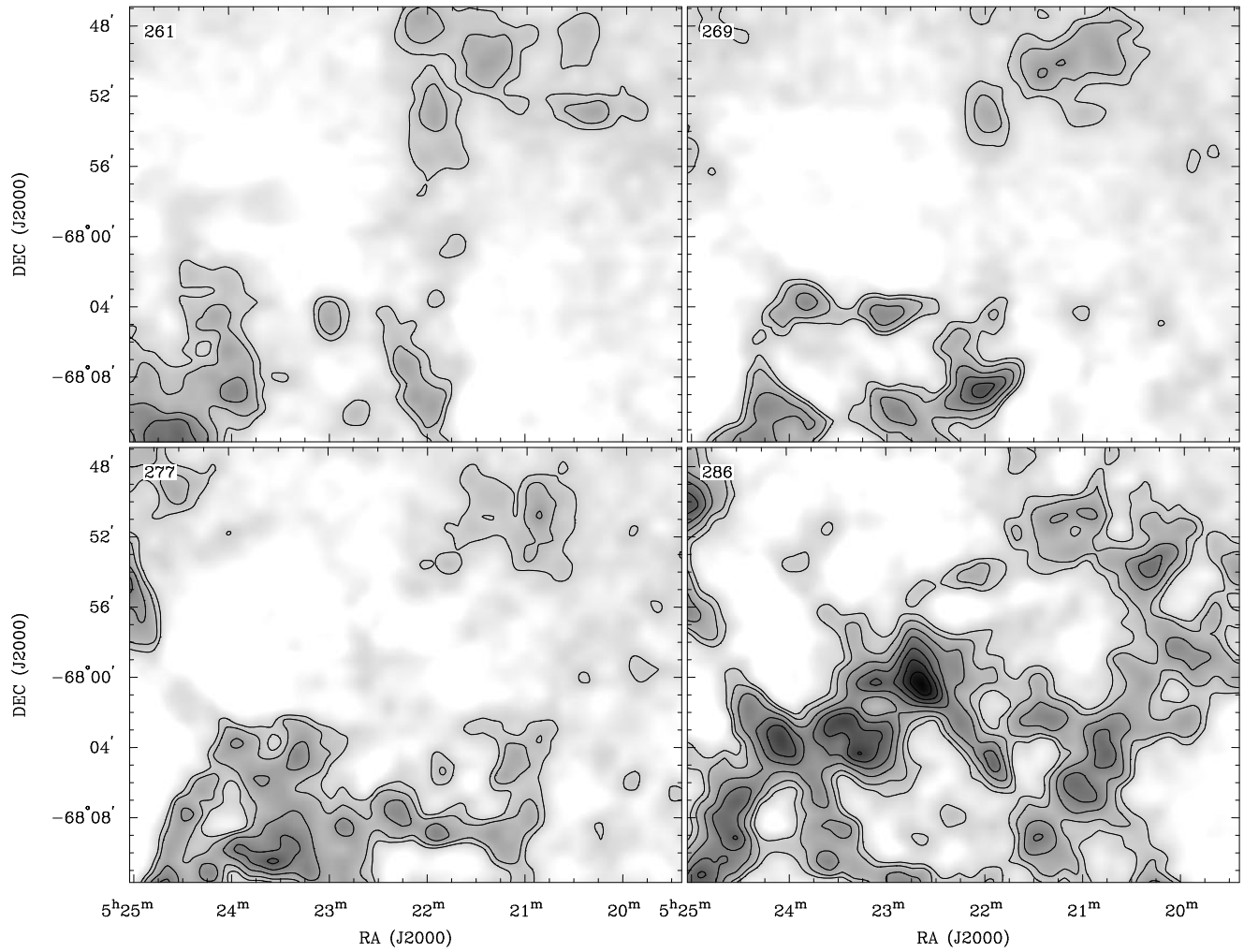



FIG. 3*a*.—*Continued*

$N(\mathrm{H\ I}) = 3.9 \times 10^{21}$ cm$^{-2}$, is a factor of 2 higher than those of adjacent regions along the rim of shell.[6]

Another example is the region at $5^h21^m58^s$, $-67°55'00''$ (J2000) bounded by Shell 1, Shell 2, and the H I hole to the north. The H I column density, $N(\mathrm{H\ I}) = 3.5 \times 10^{21}$ cm$^{-2}$, is a factor of 2 higher than those of adjacent regions along the rim of shell. It is unlikely that the H I peaks are caused by a low ionization in these directions, since the ionizing source of Shell 1 is located at the center of the shell. While we consider these H I peaks as real enhanced column densities as a result of compression between expanding shells, it is also possible that these higher surface brightness regions might be the superposition of number of features along the line of sight with the same velocity.

### 3.4. *Opening of a Breakout in* H I

A breakout in Shell 1 toward the south has been suggested by Chu et al. (1993), based on an extension of diffuse X-ray emission toward the group of H II regions associated with the OB association LH 49. This explanation has been confirmed by the presence of high-velocity ionized gas (see Fig. 1) and a lower plasma temperature in the breakout region (Magnier et al. 1996). The H I channel maps at $V_{\mathrm{hel}}$ of 300–305 km s$^{-1}$ show a clear extension of the H I hole to the southeast, coinciding with the X-ray extension. This extension of the H I hole is likely the opening through which the breakout occurs.

## 4. THE SUPERBUBBLE STRUCTURE OF SHELL 1 AND SHELL 2

Previous studies of the superbubble structure of N44 have used observations of only ionized gas (e.g., Chu et al. 1993; Magnier et al. 1996). It is found that the observed kinetic energy of the ionized Shell 1 of N44 is at least an order of magnitude lower than the value expected in Weaver et al.'s (1977) superbubble model (Magnier et al. 1996). Our new H I observation of N44 reveals the existence of a neutral gas associated with Shell 1 and possibly with Shell 2 as well. The kinetic energy of the neutral shell may alleviate the aforementioned discrepancy in energies. Below, we derive the dynamic parameters separately for the ionized and neutral components of Shell 1. The energetics of Shell 2 is discussed near the end of this section.

The expansion of Shell 1 is not uniform. Its systemic velocity, determined from the Hα velocities at the rim of the

[6] The H I velocity profile of this region has an extended red wing up to $V_{\mathrm{hel}} \sim 320$ km s$^{-1}$. However, the channel map centered at 310 km s$^{-1}$ shows an unrelated feature extending from this region to the northeast. The compression is referred to the dense clump at the systemic bulk velocity.

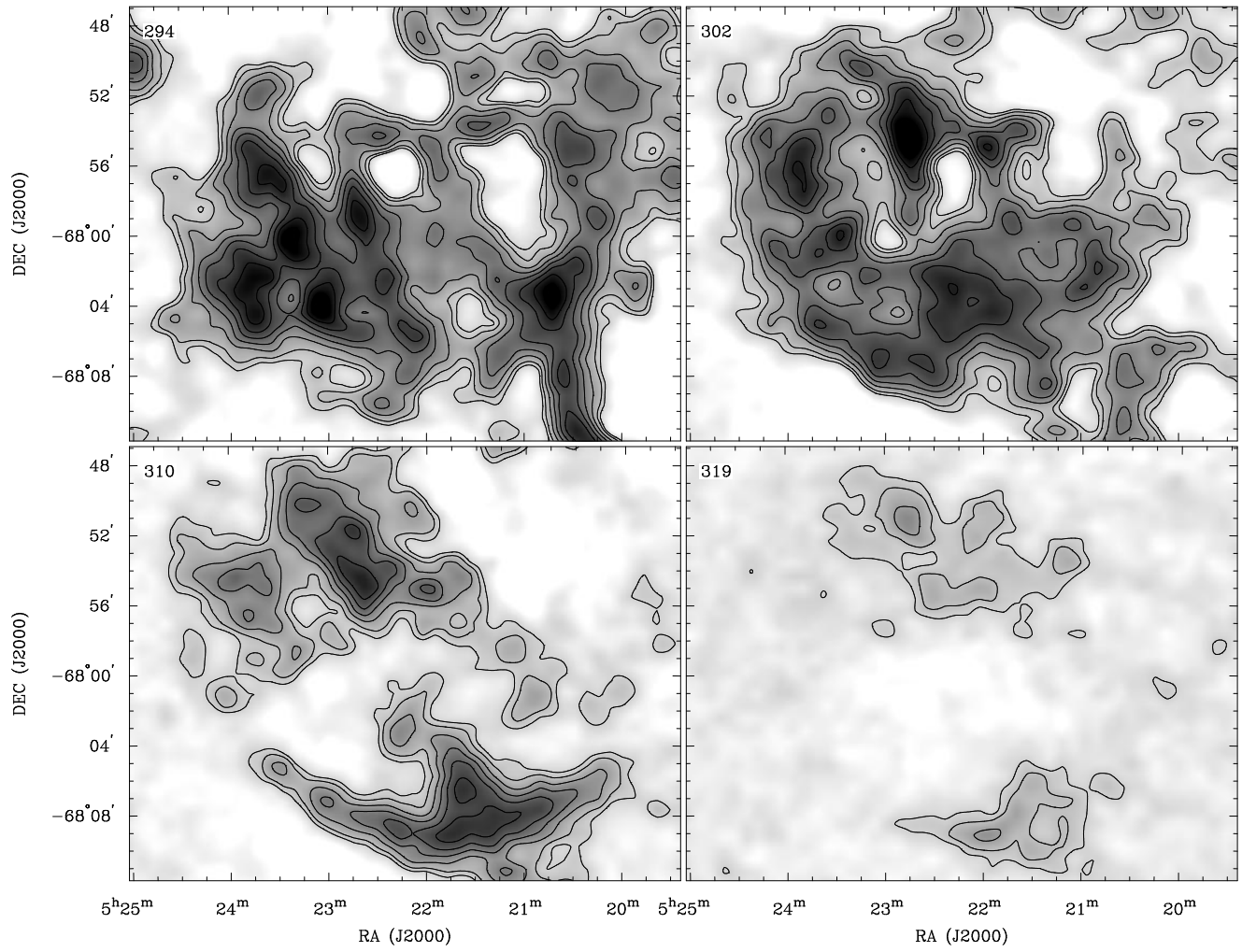



FIG. 3*a*.—*Continued*

shell, is 295–298 km s$^{-1}$. Referenced to this systemic velocity, the receding hemisphere of the ionized gas shell has an expansion velocity of 30 km s$^{-1}$ and the approaching side a velocity of 45 km s$^{-1}$. We will analyze the physical parameters of the approaching and receding hemispheres separately. These parameters are summarized in Table 2.

The H$\alpha$ echelle observation of the central region of Shell 1 shows that the receding component is 3 times as bright as the approaching component. Using photoelectrically calibrated PDS scans of the Curtis Schmidt plates of Kennicutt & Hodge (1986), together with our CCD H$\alpha$ image, we derive an emission measure of 214 cm$^{-6}$ pc for the receding component and 71 cm$^{-6}$ pc for the approaching component. To derive the rms shell density, we have assumed a uniform thin shell for Shell 1 to estimate its shell thickness. The H$\alpha$ surface brightness profile of Shell 1 shows a peak-to-center ratio of 13, indicating a fractional shell thickness $\Delta R/R = 0.02$. The FWHM of the brightness peak at the shell rim is 0.1 times the shell radius. Given the nonuniform densities, the fractional shell thickness is most likely within the range of 0.02–0.1. We have derived the rms density, mass, and kinetic energy of the shell for shell thicknesses of 0.02 and 0.1, respectively, and listed them in Table 2. The rms density in the receding hemisphere is almost twice as high as that in the approaching hemisphere, but the kinetic energy of the receding hemisphere is 21% lower than that of the approaching hemisphere. The total mass and kinetic energy of the H II shell are 2580 $M_\odot$ and $3.5 \times 10^{49}$ ergs for $\Delta R/R = 0.1$, or 1210 $M_\odot$ and $1.6 \times 10^{49}$ ergs for $\Delta R/R = 0.02$.

The H I material associated with Shell 1 of N44 shows a typical expansion structure in the position-velocity diagrams (Fig. 4) along cuts crossing the central portion of Shell 1. H I is detected in the velocity range of $V_{\rm hel} \sim$ 220–327 km s$^{-1}$. The velocity gradient of the high-velocity component in the central cuts of Shell 1 indicates an expansion motion. At the center of Shell 1, the receding side of the H I shell is expanding at a lower velocity, $28 \pm 5$ km s$^{-1}$, than the approaching side, $50 \pm 5$ km s$^{-1}$. These expansion velocities are comparable to those of the ionized component of Shell 1.

Following the analysis of the ionized shell, we discuss the receding and approaching hemispheres of the H I shell separately. The column densities, masses, and kinetic energies are listed in Table 2. The H I column density of the receding hemisphere is 2.5 times that of the approaching hemisphere, but the kinetic energy of the receding hemisphere is 21% lower. This contrast is remarkably similar to that in the H II shell. The total mass of the H I shell is 8640 $M_\odot$, and the total kinetic energy in H I is $1.1 \times 10^{50}$ ergs.

Note that the total mass and total kinetic energy of the H I component of Shell 1 are 3–7 times higher than those of

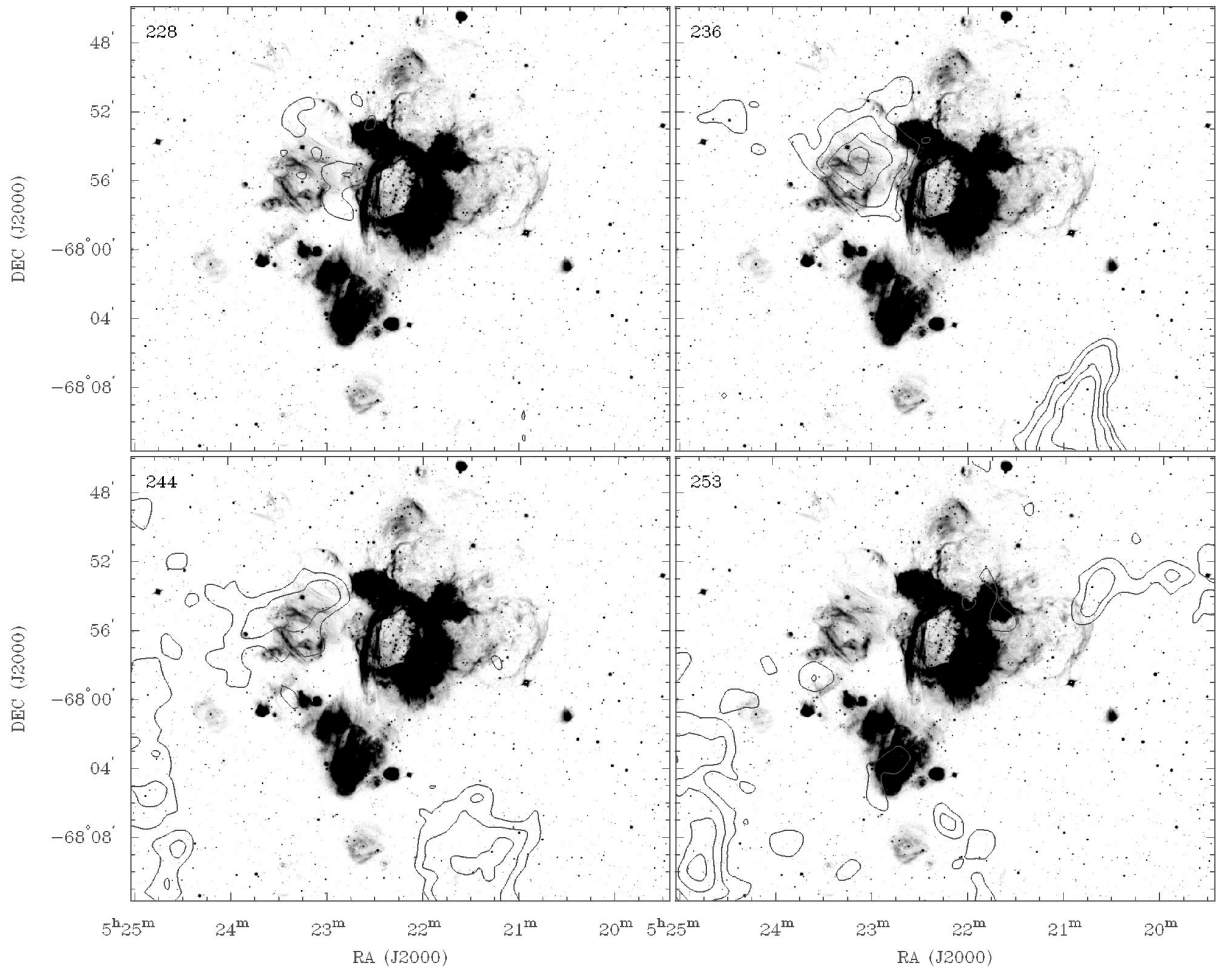



FIG. 3*b*

the H II component. This implies that analyses of superbubble dynamics *must* include the neutral gas component! Note also that the asymmetric expansion of Shell 1, shown in both H I and H II components, indicates a stratified interstellar medium with densities decreasing toward us.

The presence of molecular cloud in N44 is evidenced in the CO map by Cohen et al. (1988). CO maps made with the ESO-SEST at a higher resolution show molecular material associated with the B, C, and D components of N44, the compact H II regions along the west (the B component) and southwest (the C component) rim of Shell 1 and to the southeast (the D component, associated with LH 49) of Shell 1 (Israel et al. 1993; Chin et al. 1997). Contour maps of N44BC (Chin et al. 1997) in $^{12}$CO ($J = 1$–0) show a peak at $5^{h}22^{m}00^{s}.9$, $-67°57'59''.9$ (J2000), at $V_{LSR} = 283$ km s$^{-1}$ or $V_{hel} = 295.6$ km s$^{-1}$. This velocity agrees well with the systemic velocity of H I and H II emission.

Unfortunately, there is no detailed CO map over the entire N44 complex. Chin et al. (1997) use virial arguments to suggest that the molecular mass of N44BC may be as high as $10^5\ M_\odot$, a factor of $\sim 10$ higher than the H I mass of N44 Shell 1! However, N44BC are concentrations near the periphery of Shell 1, and it is uncertain whether this molecular gas participates in the expansion of Shell 1. Clearly, detailed distribution of molecular gas in N44 needs to be mapped in order to determine whether the molecular gas plays an important role in the superbubble dynamics.

We may reexamine the energetics of Shell 1 with the additional H I information. The total stellar wind and supernova energy input implied by the observed stellar content (Oey & Massey 1995), the total kinetic energy derived in this paper, and the thermal energy of the hot interior derived from X-ray observations (Magnier et al. 1996) are summarized in Table 2. In a pressure-driven superbubble, the thermal and kinetic energies are expected to be 35/77 and 15/77 times the total mechanic energy input from stellar winds and supernovae (Weaver et al. 1977; Mac Low & McCray 1988). The expected thermal energy and shell kinetic energy are also listed in Table 2. The observed shell kinetic energy is dominated by that of the expanding H I shell; still, there is at least a factor of 5 discrepancy between the observed and expected kinetic energies. The discrepancy might be caused by the breakout of Shell 1, since a large fraction of the stellar energy input may have been lost in the breakout. Other possibilities are discussed in § 6.2.

The superbubble Shell 2 of N44 is very different from Shell 1. We use the observations by Meaburn & Laspias (1991) and Hunter (1994) to discuss the expansion of the ionized gas in Shell 2. These observations clearly show that the expansion of Shell 2 is not as well defined as that of Shell

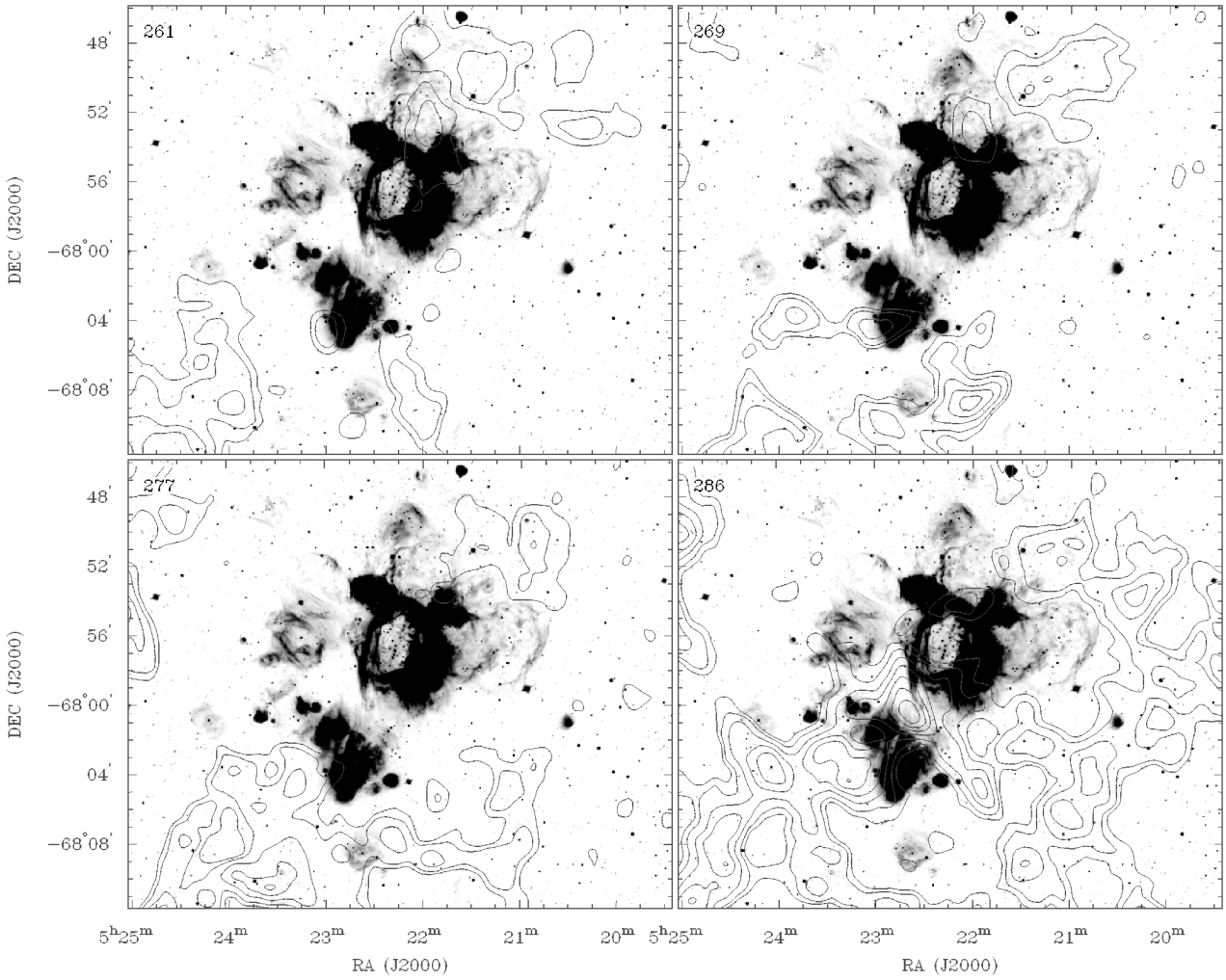



FIG. 3b.—*Continued*

1. Meaburn & Laspias (1991) find that the radial velocities of Shell 2 change from 304 km $s^{-1}$ at the edge to 320 km $s^{-1}$ at the center. They suggest that this is the receding side of the superbubble and the faint approaching side is not detected. Hunter (1994) has observed three slit positions in Shell 2: positions 1, 2E1, and 2E2. The velocities along the slit position 2E1, near the center of Shell 2, are redshifted by up to 10 km $s^{-1}$ from the systemic velocity, qualitatively confirming the results of Meaburn & Laspias (1991). Along the slit 1, across the western rim of Shell 2, the main velocity component shows irregular velocities with blueshifts of up to $-60$ km $s^{-1}$ from the systemic velocity. The slit position 2E2 shows an apparent faint component blueshifted from the main component by about $-80$ km $s^{-1}$; however, Hunter (1994) has neither discussed the validity of this faint component (as opposed to an instrumental artifact) nor reported it in her Table 5. These observations are adequate in establishing an expansion motion in Shell 2, but the spatial coverage is too sparse to allow an accurate derivation of dynamic parameters of the ionized gas in Shell 2.

The H I observations of Shell 2, having a complete spatial coverage, are better suited for analysis of the expansion of Shell 2. The H I gas in Shell 2 shows an H I hole in the channel maps as well as in the position-velocity diagrams (Fig. 4). The receding side of the shell is detected along some cuts across the shell. The expansion velocity of the receding part of the H I shell is $30 \pm 5$ km $s^{-1}$, higher than that of the ionized gas shell (Meaburn & Laspias 1991). The approaching side is much fainter; only a bright, high-velocity H I knot is detected. (The rest of the approaching hemisphere is probably below our detection limit.) The expansion velocity of the approaching side of the H I shell is $50 \pm 5$ km $s^{-1}$, comparable to that of the ionized gas shell implied by Hunter's slit position 1 and lower than that implied by Hunter's slit position 2E1, if the faint blueshifted component is real. This asymmetric expansion of the H I and H II gas in Shell 2 is similar to that of Shell 1; therefore, Shell 1 and Shell 2 probably share the same interstellar environment.

In a similar way, we derive the physical parameters of the H I component of Shell 2, treating the approaching and receding sides separately. The H I mass of Shell 2 is 5850 $M_\odot$ in the receding hemisphere and 3090 $M_\odot$ in the approaching hemisphere. The total kinetic energy of the H I in Shell 2 is $1.3 \times 10^{50}$ ergs, 20% higher than that of the H I in Shell 1. The stellar content of Shell 2 has not been as well studied as that of Shell 1, and the X-ray observations of Shell 2 have much lower S/N ratios, hence Shell 2 cannot be modeled in as much detail as Shell 1.

## 5. THE PHYSICAL STRUCTURE OF SNR 0523−679

SNR 0523−679, centered at $5^h23^m06^s$, $-67°53'15''$

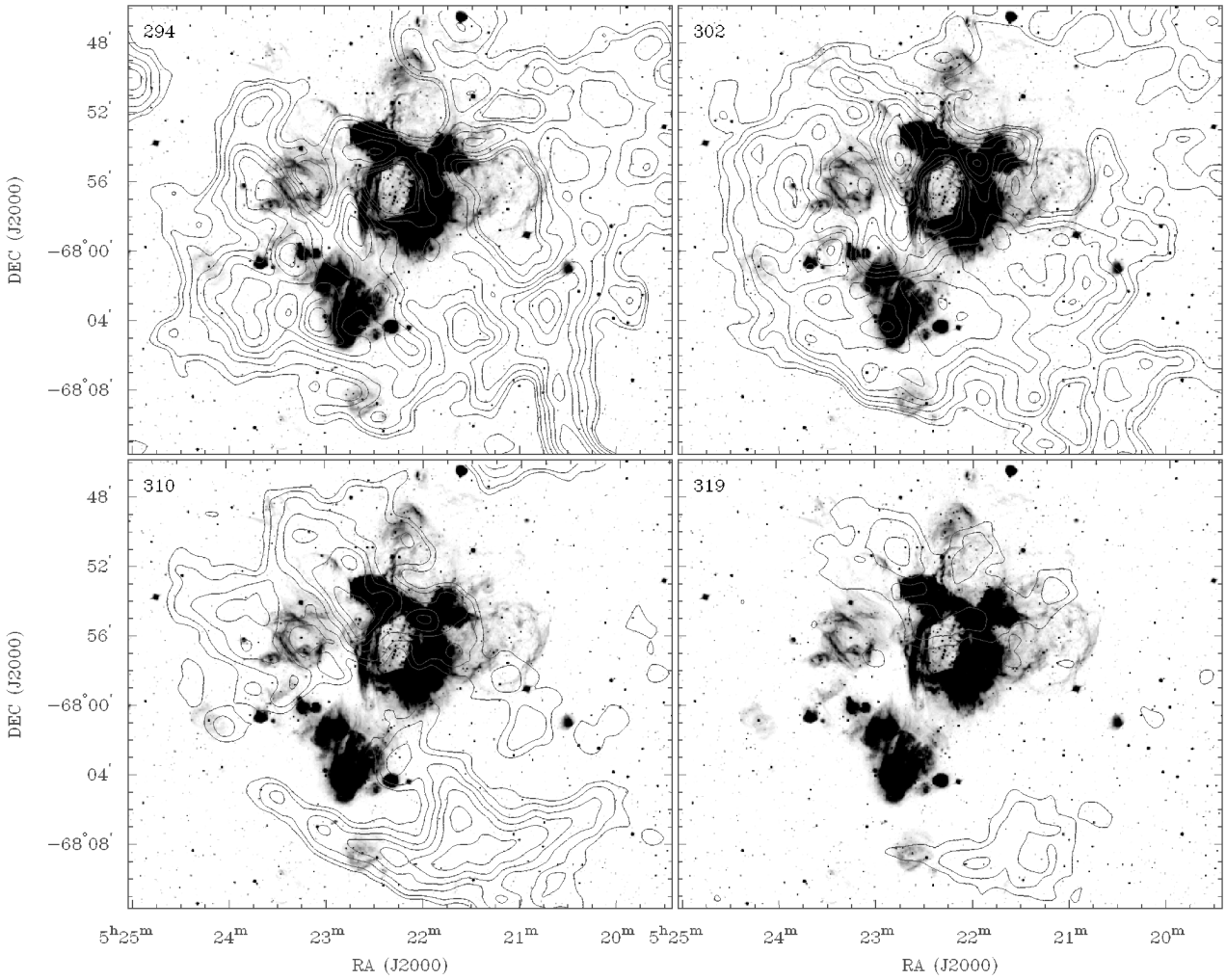



FIG. 3b.—*Continued*

(J2000), was first diagnosed by its diffuse X-ray emission (Chu et al. 1993). The diffuse X-ray emission is surrounded by curved Hα filaments that are suggestive of a shell with a diameter of ∼3′.8. The Hα shell, called Shell 3 by Chu et al. (1993), is bounded by H II regions on the west and south sides. The bright arc on the west side of the shell is also on the surface of the H II region around the OB association LH 48, indicating a physical interaction between the SNR and the H II region. The southern part of the SNR shell is blended with a diffuse ringlike H II region; however, it is not clear whether they physically interact. Within the boundary of the SNR shell, long Hα filaments and dust lanes run from the northeast corner to the southwest corner, dissecting the shell into two lobes. The X-ray emission shows a corresponding two-lobe structure, which could be caused by the absorption in the dust lane.

The internal motion of the SNR is revealed in the echellograms at slit positions S4 and S5 (Fig. 1). The velocities at the shell rim sampled by these two slits are $V_{\rm hel} = 297$–$304$ km s$^{-1}$, which will be adopted as the systemic velocity of the ionized SNR shell. The echellograms show very different velocity structures in the north and south lobes of the SNR. The north lobe shows prominent blueshifted material in the Hα line; the brighter parts have velocity offsets up to $-125$ km s$^{-1}$, while the fainter parts have velocity offsets up to $-150$ km s$^{-1}$. The receding side of the north lobe has much smaller velocity offsets, ∼20 km s$^{-1}$. The south lobe shows mostly redshifted material in the Hα line, with velocity offsets up to $+100$ km s$^{-1}$; however, blueshifted material is also detected at the northern end of the south lobe, with velocity offsets up to $-100$ km s$^{-1}$.

For such an irregular pattern of expansion, it is impossible to determine the kinetic energy of the ionized gas in SNR 0523−679 using our limited echelle observations. We can nevertheless assume a uniform shell and derive upper limits on the mass and kinetic energy. The brightest part of the SNR along slit S5 has an emission measure of 25 cm$^{-6}$ pc. The apparent width of the SNR shell, 6″.5 or 1.6 pc, provides an upper limit on the real shell thickness. The corresponding rms $n_e$ is ∼4 cm$^{-3}$. The upper limits on the mass and kinetic energy are thus 370 $M_\odot$ and $6 \times 10^{49}$ ergs.

The H I gas associated with SNR 0523−679 has a very different velocity structure from that of the ionized gas described above. The bulk velocity of H I gas toward the SNR is $V_{\rm hel} = 306 \pm 5$ km s$^{-1}$. Since this velocity is similar to the SNR's systemic velocity determined with the Hα line, we will adopt this velocity as the systemic velocity of the H I gas associated with the SNR. The channel maps in Figure 3 show an H I hole at $V_{\rm hel} = 297$ km s$^{-1}$, although the size of the H I hole is smaller than that of the Hα shell.

The receding side of the H I gas associated with the SNR is clearly seen in the channel map at $V_{\rm hel} = 325$ km s$^{-1}$,

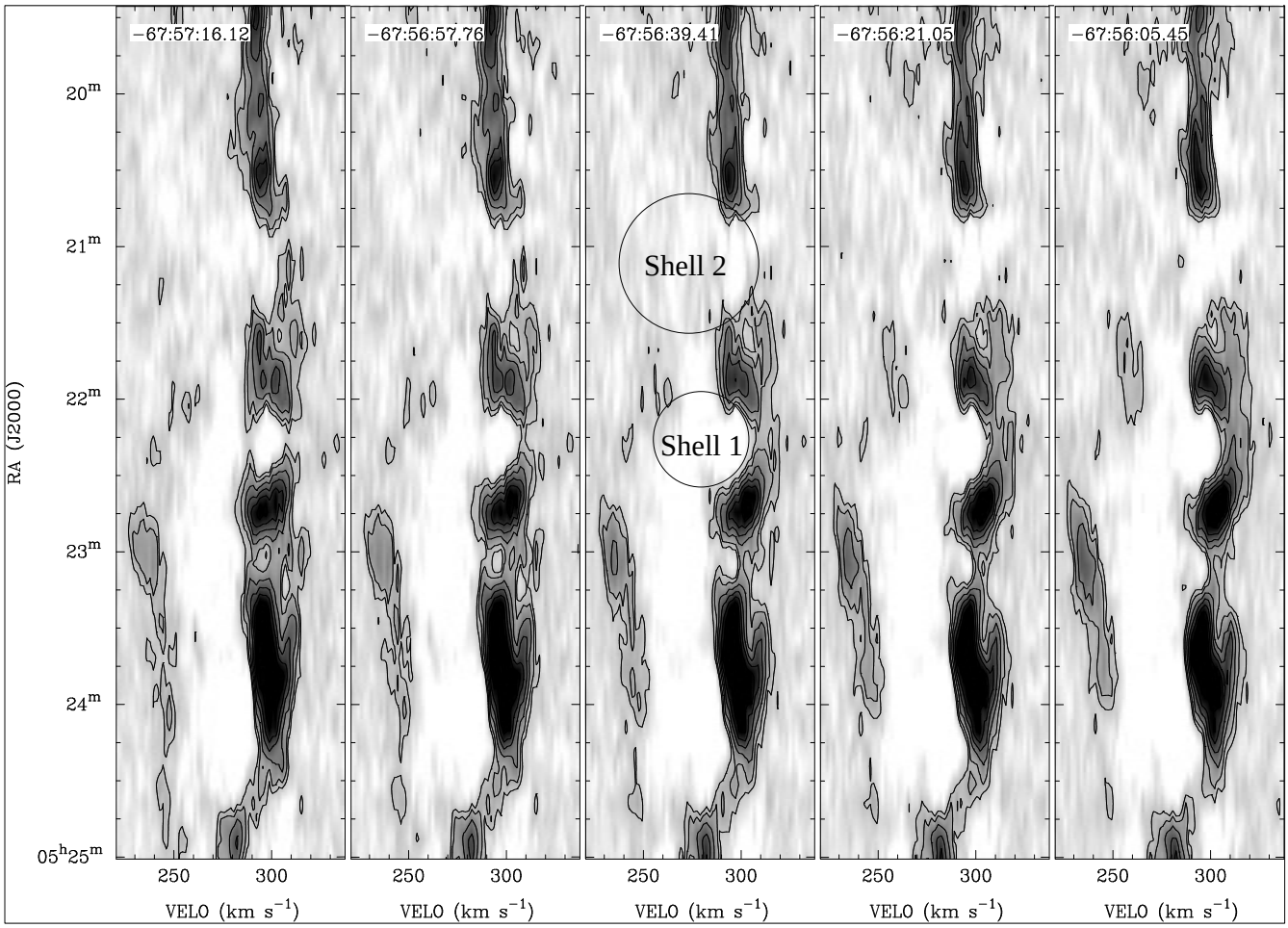



FIG. 4.—Position-velocity plots of H I in the N44 complex. The contours correspond to the associated pixel brightness $\geq 2.5\ \sigma$. The high-velocity gas associated with the SNR might have an unresolved gas component, which is related to an H$\alpha$ blister on the periphery of Shell 1.

suggesting an expansion velocity of 20–30 km s$^{-1}$. The approaching side of the H I gas is more complex. Blue-shifted H I gas in the velocity range $V_{\rm hel} = 230$–$245$ km s$^{-1}$ is seen toward the SNR. However, this H I gas also extends farther south than the boundary of the SNR; the southern extension is particularly pronounced in the region between the SNR and Shell 1 at $V_{\rm hel} = 228$–$235$ km s$^{-1}$. As we explained in § 3, Shell 1 might be responsible for the acceleration of the high-velocity H I in the region between Shell 1 and the SNR. Interestingly, the highest velocity ($V_{\rm hel} = 226$ km s$^{-1}$) H I component unambiguously associated with the SNR is located at the northeastern edge, instead of the center, of the optical shell. This might indicate that a breakout similar to that seen at the south edge of Shell 1 has occurred at this position.

We may estimate the mass and kinetic energy of the H I gas associated with the SNR. The high-velocity H I gas is more extended than the optical boundary of the SNR. To exclude the contribution from other sources, we use only the part of H I gas projected within the optical boundary of the SNR. The mass of the approaching side of the H I gas is $7460 \pm 1000\ M_\odot$, and the kinetic energy of the SNR is $2.7 \times 10^{50}$ ergs. The mass and kinetic energy of the H I gas are much higher than those of the ionized gas in the SNR. This is similar to what we have found for the superbubble Shell 1.

The thermal energy of the SNR can be derived from the *ROSAT* and *ASCA* observations in X-rays. The best Raymond & Smith (1977) model fits of these two sets of data give very different plasma temperature and absorption column density; however, the thermal energies derived from these two sets of parameters are similar. The best fit to the *ROSAT* Position Sensitive Proportional Counter data (Chu et al. 1993) gives a plasma temperature of $kT = 0.835$ keV, an absorption column density of $\log N_{\rm H} = 20.68$, and a normalization factor of $\log N_e^2\, Vf/4\pi D^2 = 10.817$, in the cgs units, where $N_e$ is the electron density, $V$ is the volume, $f$ is the volume filling factor, and $D$ is the distance. The thermal energy of the SNR calculated from this model fit is $1.2 \times 10^{50}(f/0.5)^{1/2}$ ergs. The best fit to the *ASCA* Solid-State Imaging Spectrometers (SIS) data gives $kT = 0.35$ keV, $\log N_{\rm H} = 21.48$, and $\log N_e^2 Vf/4\pi D^2 = 11.326$. The thermal energy from this model fit is $9.0 \times 10^{49}(f/0.5)^{1/2}$ ergs. Considering the uncertainties of filling factor and spectral fits, the thermal energy of the SNR is probably $(1.0 \pm 0.5) \times 10^{50}$ ergs.

The thermal energy in SNR 0523−679 is similar to that in each of the shells in the SNR DEM L 316 (Williams et al. 1997), despite the fact that SNR 0523−679 is in a much more inhomogeneous medium and has a much more non-uniform expansion. The kinetic energy in the ionized gas of SNR 0523−679 is of a similar order of magnitude as the

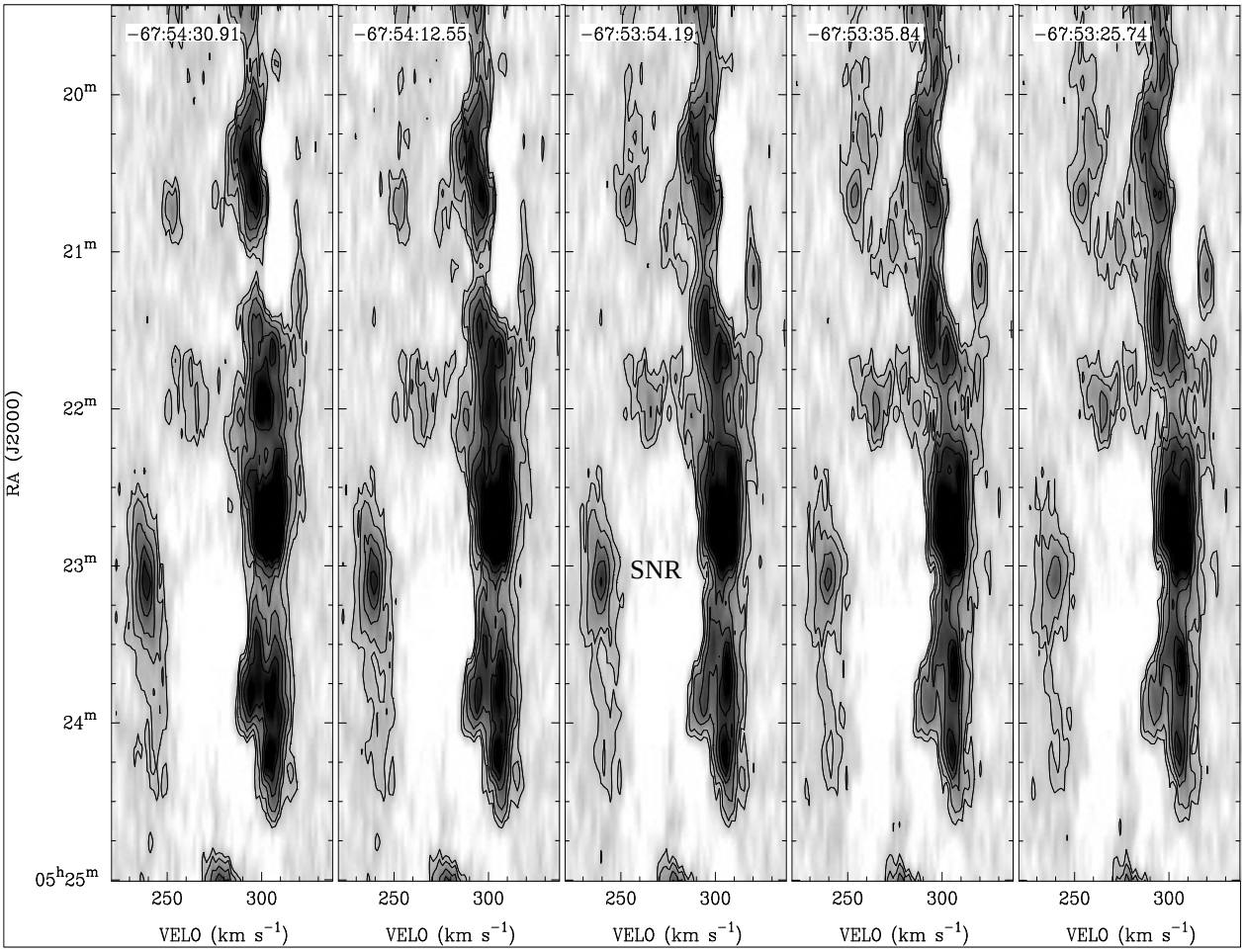



FIG. 4.—*Continued*

thermal energy of SNR 0523−679. This behavior is similar to what is observed in DEM L 316. The total kinetic energy (H I + ionized) of SNR 0523−679 is much larger than the thermal energy in the SNR's hot interior. This behavior is similar to what is seen in N44's superbubble Shell 1.

## 6. DISCUSSION

### 6.1. *Implications for the* H I *Structure of the LMC*

The ATCA H I survey of the LMC (Kim & Staveley-Smith 1997) shows H I holes with sizes ranging from a few tens of pc to ~1400 pc. It is conceivable that these H I holes have been created by the combined effects of fast stellar winds and supernova explosions. However, most of these holes do not have any recognizable stellar content or corresponding ionized gas shells, making follow-up studies difficult, if not impossible. N44, containing three OB associations at three different evolutionary stages, offers an ideal site for us to study how massive stars shape the interstellar medium. The current H I structure in N44 is readily visible, whereas the ionized gas structure allows us to foresee the future H I structure after the ionizing fluxes have terminated at the demise of all massive stars in N44. From the study of N44, we hope to gain insight into the general H I structure of the LMC.

We first examine the validity of the apparent "holes" in the H I maps of N44. The integrated H I map of N44 shows two deep depressions. Both depressions have associated H I shells, and both shells have optical counterparts, the superbubbles Shell 1 and Shell 2. For Shell 1, the H I shell and the ionized gas shell have similar expansion patterns and velocities: both have the far side receding at 30 km $s^{-1}$ and the near side approaching at 45–50 km $s^{-1}$. For Shell 2, the H I shell may expand faster than the ionized gas shell in the receding side, 30 km $s^{-1}$ versus less than 20 km $s^{-1}$; the comparison is more uncertain on the approaching side. The different behavior of Shell 1 and Shell 2 might be an artifact of insufficient optical observations of the ionized gas in Shell 2 (as described in § 4), or caused by the different distribution of ionizing sources. Shell 1 has a central ionizing source, the OB association LH 47, hence its neutral H I shell is adjacent and exterior to its ionized gas shell. Shell 2, on the other hand, has no central OB association, and its ionizing flux might be provided by LH 47's O stars to the east of Shell 2. The structure of the ionized gas in Shell 2 thus depends on the relative locations of the ionizing stars and would not have a one-to-one correspondence with the neutral H I gas shell.

The channel maps of H I in N44 also show numerous holes. The most obvious H I holes are present in the map centered at the bulk velocity of N44, $V_{\rm hel} = 297$ km $s^{-1}$. In addition to the aforementioned superbubbles Shell 1 and Shell 2, two other holes are present to the north. As described in § 3, one of these H I holes has Hα filaments delineating a shell structure, while the other has no evidence of a coherent shell structure in Hα images. These two H I

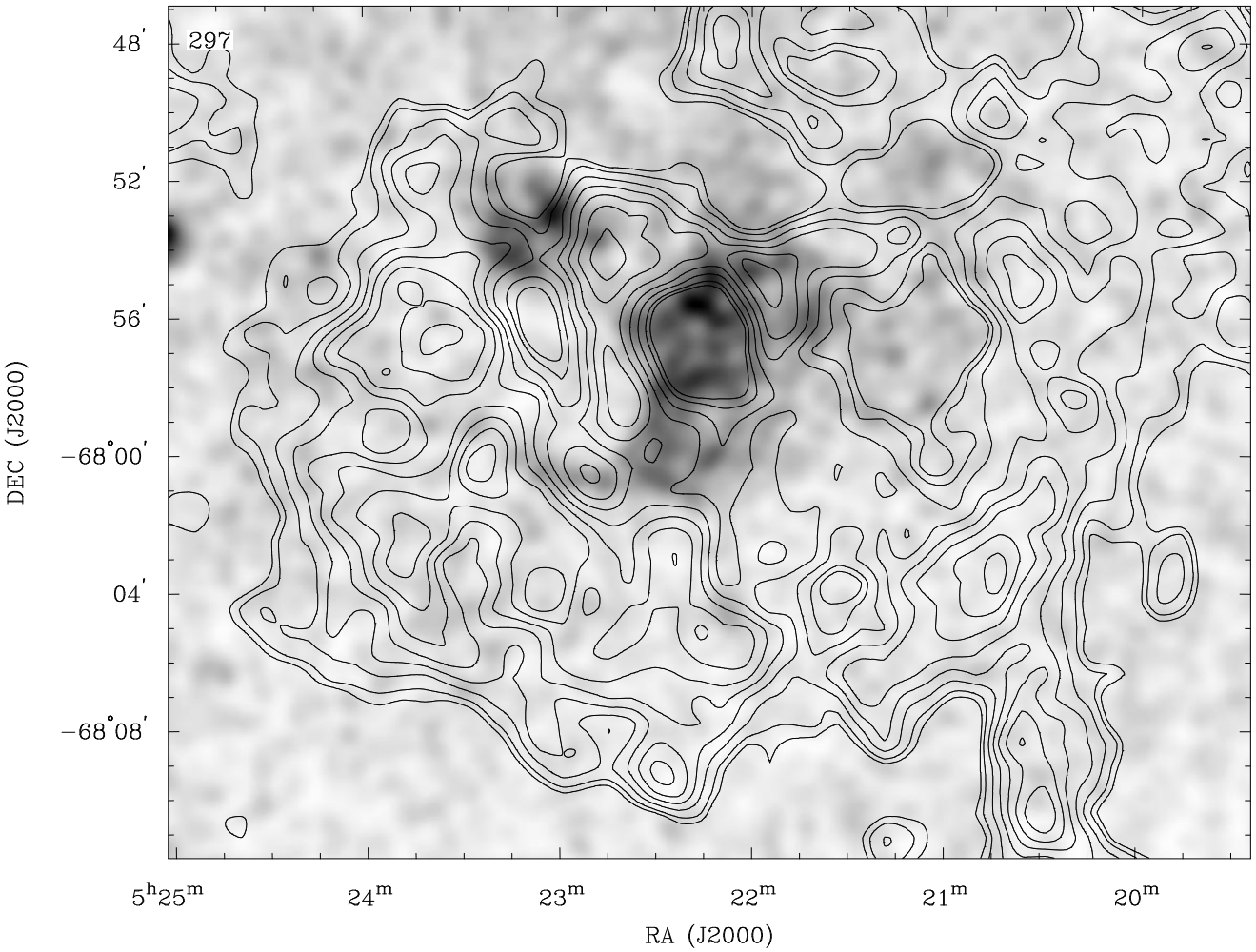



FIG. 5.—H I contours overplotted on an X-ray image of N44. The H I contours are derived from the channel map centered at $V_{hel} = 297$ km s$^{-1}$. The H I contour levels are 0.07, 0.10, 0.15, 0.20, 0.25, 0.30, 0.35, 0.40, and 0.45 Jy beam$^{-1}$. The X-ray image is a smoothed *ROSAT*/PSPC image from Chu et al. (1993).

holes must be real holes, as both regions show enhanced X-ray emission (see Fig. 5), indicating that the holes are filled with $10^6$ K hot gas. It might be argued that the enhanced X-ray emission is resultant from a smaller foreground absorption. Since the integrated H I map does not show obvious anticorrelation between H I column density and X-ray surface brightness in N44, we consider this argument unlikely. These apparent H I holes in the channel maps must correspond to real cavities.

Conversely, we next examine the H I maps for holes at regions where we expect them. The SNR 0523−679, having a diameter of ∼4′, is well resolved by our H I maps. However, only a very shallow depression in H I column density is present in the integrated H I map or the channel map centered at 297 km s$^{-1}$. This is perhaps understandable because the SNR 0523−679 is in a low-density medium, indicated by its fast expansion and large size. The H I gas that has been accelerated by the SNR also shows a patchy structure, consistent with a low-density medium around the SNR.

We may also expect H II regions to show up as holes in H I maps. However, neither the H II region around LH 48 nor the H II region around LH 49 shows a hole in the integrated or channel maps of H I. The lack of correspondence between young H II regions and H I distribution indicates that the star formation must have taken place in molecular clouds, as opposed to H I clouds. Thus, both the H I and the H II gases are produced by photodissociation and photoionization of the molecular gas. This conclusion has been previously reached by Allen, Atherton, & Tilanus (1986) based on their H I observations of the spiral galaxy M83.

Besides H I holes and expanding shells, we see clear evidence of acceleration of H I gas by superbubbles or SNRs, compression of H I gas between expanding shells, and breakout structures in N44. Similar phenomena must exist in other active star-forming regions. It is conceivable that the interstellar medium has been shaped by multiple episodes of massive star formation, and that the complex H I structure represents the cumulative effects of the previous massive star formation.

### 6.2. H I *Shell and Superbubble Dynamics*

The most remarkable lesson that we have learned from the H I study of superbubbles in N44 is that the neutral gas actually contains more mass and kinetic energy than the ionized gas! For example, in Shell 1 of N44, the mass and kinetic energy in the expanding H I shell is 3–7 times those of the ionized gas shell. Thus, the H I gas is an important component in superbubbles. Previously, superbubble

TABLE 2

PHYSICAL PARAMETERS OF SHELL 1 AND SHELL 2

| PARAMETER | SHELL 1[a] | | SHELL 1[b] | | SHELL 2 | |
|---|---|---|---|---|---|---|
| | Front | Back | Front | Back | Front | Back |
| **H II Hemisphere** | | | | | | |
| Shell thickness (pc) | 0.5 | 0.5 | 2.3 | 2.3 | ... | ... |
| $n_e$ (cm$^{-3}$) | 11.9 | 20.7 | 5.6 | 9.7 | ... | ... |
| Mass ($M_\odot$) | 440 | 770 | 950 | 1630 | ... | ... |
| $V_{exp}$ (km s$^{-1}$) | 45 | 30 | 45 | 30 | ... | ... |
| $E_{kin}$ ($10^{49}$ ergs) | 0.89 | 0.68 | 1.9 | 1.5 | ... | ... |
| **H I Hemisphere** | | | | | | |
| $N$(H I) ($10^{20}$ cm$^{-2}$) | 3.6 | 1.4 | | | 1.6 | 3.0 |
| Mass ($M_\odot$) | 6180 | 2460 | | | 3090 | 5850 |
| $V_{exp}$ (km s$^{-1}$) | 28 | 50–60 | | | $50 \pm 5$ | $30 \pm 5$ |
| $E_{kin}$ ($10^{49}$ ergs) | 4.8 | 6.1 | | | 7.7 | 5.2 |
| **The Whole Shell** | | | | | | |
| H II $E_{kin}$ ($10^{49}$ ergs) | 1.6–3.4 | | | | | |
| H I $E_{kin}$ ($10^{49}$ ergs) | 11 | | | | 13 | |
| Total $E_{kin}$, observed ($10^{49}$ ergs) | 13–14 | | | | | |
| $E_{th}$, observed in shell ($10^{49}$ ergs) | 3–20 | | | | | |
| $E_{th}$, observed in shell & breakout ($10^{49}$ ergs) | 13–30 | | | | | |
| Wind and SN energy input ($10^{49}$ ergs) | 400–700 | | | | | |
| Total $E_{kin}$, expected ($10^{49}$ ergs) | 78–136 | | | | | |
| $E_{th}$, expected ($10^{49}$ ergs) | 200–300 | | | | | |

[a] With an ionized shell thickness $\Delta R/R = 0.02$.
[b] With an ionized shell thickness $\Delta R/R = 0.1$.

dynamics has been observed with optical emission lines, hence only the ionized gas shells have been considered. This clearly needs to be improved.

It has been a long-standing problem that the observed kinetic energy in a wind-blown bubble is much too low compared to that expected from Weaver et al.'s (1977) pressure-driven bubble model (Oey & Massey 1995). We have summed the kinetic energy in the ionized gas shell and in the H I shell for the superbubble Shell 1 in N44, finding that the observed total kinetic energy is still at least a factor of 5 lower than expected. The observed ratio of kinetic energy to thermal energy is nevertheless closer to the theoretical value of 3/7, especially if the thermal energy in the breakout region is included.

The superbubble dynamics of Shell 1 may have been significantly altered by the energy loss through the breakout; however, the breakout may not be the only cause of the discrepancy between the observed superbubble dynamics and theoretical predictions. The fact that the age of the OB association LH 47, $\geq 10$ Myr (Oey & Massey 1995), is much larger than the dynamic age of Shell 1, less than 1 Myr, indicates that the formation of a superbubble did not start as soon as the central OB association was formed. It is possible that LH 47 was formed in a molecular cloud, and the currently visible superbubble Shell 1 did not start to expand rapidly until it had broken out of the molecular cloud. This hypothesis is supported by the remnant molecular clouds observed toward N44 (Israel et al. 1993; Chin et al. 1997). Only the youngest H II regions are still associated with molecular material, and these youngest H II regions show neither H I holes nor H II shell structures. Similar explanations have been proposed for the superbubble in N11 and may be common among all superbubbles (Mac Low et al. 1998).

Of course, off-center SNR shocks could have provided acceleration and contributed to the discrepancy between the observed superbubble dynamics and the theoretical predictions. Evidence of SNR shocks in N44 includes the excess X-ray emission (Chu et al. 1993) and strong [S II]/H$\alpha$ ratios (Hunter 1994). Future observational studies of superbubble dynamics need to include both the neutral and ionized gas components and to extend to superbubbles with a wide range of X-ray luminosities, so that additional SNR acceleration effects can be differentiated from normal superbubble dynamics.

We thank the team members of the H I survey project, R. Sault, K. C. Freeman, M. A. Dopita, M. J. Kesteven, D. McConnell, and M. Bessell. S. K. would like to thank P. R. Wood for useful comments that helped improve the paper and J. Mould and MSSSO for financial support making the collaborative visit to Illinois possible. We also thank the anonymous referee for making suggestions to improve the paper. Y. H. C. acknowledges NASA grants NAG 5-3246 (LTSA) and NAG 5-1900 (*ROSAT*). R. C. S. acknowledges NSF grant AST 95-30747 and the Dean B. McLaughlin Fund at the University of Michigan.

REFERENCES

Allen, R. J., Atherton, P. D., & Tilanus, R. P. J. 1986, Nature, 319, 296
Chin, Y.-N., Henkel, C., Whiteoak, J. B., Millar, T. J., Hunt, M. R., & Lemme, C. 1997, A&A, 317, 548
Chu, Y.-H., & Mac Low, M.-M. 1990, ApJ, 365, 510
Chu, Y.-H., Mac Low, M.-M., García-Segura, G., Wakker, B., & Kennicutt, R. C., Jr. 1993, ApJ, 414, 213
Cohen, R. S., Dame, T. M., Garay, G., Montani, J., Rubio, M., & Thaddeus, P. 1988, ApJ, 331, L95

Henize, K. G. 1956, ApJS, 2, 315
Hunter, D. 1994, AJ, 107, 565
Israel, F.P., et al. 1993, A&A, 276, 25
Kennicutt, R. C., & Hodge, P. W. 1986, ApJ, 306, 130
Kim, S., & Staveley-Smith, L. 1997, in Star Formation Near and Far (Maryland: AIP), in press
Kim, S., Staveley-Smith, L., Dopita, M. A., Freeman, K.C., Sault, R. J., Kesteven, M.J., & McConnell, D. 1998, ApJ, 503, 674
Lucke, P. B., & Hodge, P. W. 1970, AJ, 75, 171
Mac Low, M.-M., Chang, T. H., Chu, Y.-H., Points, S. D., Smith, R. C., & Wakker, B. P. 1998, ApJ, 493, 260
Mac Low, M.-M., & McCray, R. 1988, ApJ, 324, 776
Magnier, E. A., Chu, Y.-H., Points, S. D., Hwang, U., & Smith, R. C. 1996, ApJ, 464, 829
McKee, C. F., & Ostriker, J. P. 1977, ApJ, 218, 148
Meaburn, J., & Laspias, V. N. 1991, A&A, 245, 635
Norman, C. A., & Ikeuchi, S. 1989, ApJ, 345, 372
Oey, M. S., & Massey, P. 1995, ApJ, 452, 216
Raymond, J. C., & Smith, B. W. 1977, ApJS, 35, 419
Sramek, R. A., & Schwab, F. R. 1989, in Synthesis Imaging in Radio Astronomy, ed. Perley, R. A., Schwab, F. R., & Bridle, A. H. (San Francisco: ASP), 123
Wang, Q., & Helfand, D.J. 1991, ApJ, 373, 497
Weaver, R., McCray, R., Castor, J., Shapiro, P., Moore, R. 1977, ApJ, 218, 377
Williams, R. M., Chu, Y.-H., Dickel, J. R., Beyer, R., Petre, R., Smith, R. C., & Milne, D. K. 1997, ApJ, 618